

## RESEARCH

## ICE SHEETS

## Hidden cascades of seismic ice stream deformation

Andreas Fichtner<sup>1\*</sup>, Coen Hofstede<sup>2</sup>, Brian L. N. Kennett<sup>3</sup>, Anders Svensson<sup>4</sup>, Julien Westhoff<sup>4</sup>, Fabian Walter<sup>5,6</sup>, Jean-Paul Ampuero<sup>7</sup>, Eliza Cook<sup>4</sup>, Dimitri Zogone<sup>8</sup>, Daniela Jansen<sup>2</sup>, Olaf Eisen<sup>2,8,9</sup>

Ice streams are major regulators of sea level change. However, standard viscous flow simulations of their evolution have limited predictive power owing to incomplete understanding of involved processes. On the Greenland ice sheet, borehole fiber-optic observations revealed a brittle deformation mode that is incompatible with viscous flow, over length scales similar to the resolution of modern ice sheet models: englacial ice quake cascades that are unobservable at the surface. Nucleating near volcanism-related impurities that promote grain boundary cracking, the ice quake cascades appear as a macroscopic form of crystal-scale wild plasticity. A conservative estimate indicates that seismic cascades are likely to produce strain rates that are comparable in amplitude with those measured geodetically, providing a plausible missing link between current ice sheet models and observations.

Ice streams strongly affect the total mass balance of the Antarctic and Greenlandic ice sheets (1–3). The need to predict their behavior in a changing climate and the concomitant consequences for human society motivates the development of ice sheet simulations (4). The predictive power of such simulations—for example, in terms of projected sea level rise or ice sheet retreat rates—is limited by various aspects of existing numerical models, including numerical discretization and rheology as well as material, hydraulic, and stress-strain conditions at the base (3, 5, 6). To date, how-

ever, knowledge of model boundary conditions and rheology is largely limited by the difficulty to perform in situ measurements of glacial properties and processes. We used distributed acoustic sensing (DAS) (7, 8) to detect a mode of ice deformation that cannot be reconciled with the commonly used nonlinear viscous rheology of Glen's flow law (9): cascading englacial thrust faulting, observed near the borehole of the East Greenland Ice Core Project (EastGRIP) on the Northeast Greenland Ice Stream (NEGIS) (Fig. 1, A and B). Accounting for ~12% of its total mass discharge (1, 10),

NEGIS is the largest ice stream of the Greenland Ice Sheet and a major contributor to current sea level rise (2), which underlines the importance of understanding its rheology and deformation mechanisms. In this context, ice core crystallography at EastGRIP has been studied extensively by use of both in situ observations (11) and remote geophysical methods (12)—for example, to link variations in crystal orientation to large-scale viscous flow patterns (13). Optical line scanning has produced images of structures very similar to geological fault-bend folds on thrust ramps, which is a type of thrust structure (Fig. 1C) (14) that has not been observed in ice cores before (15). Although they evidence that shortening was accommodated by brittle deformation structures in the past, their current activity and contribution to ice deformation remain elusive.

We lowered a loose-tube fiber-optic cable, containing four single-mode fibers, 1500 m into the EastGRIP borehole, which had reached a depth of 2420 m at that time (Fig. 1B). For 14 hours, on 10 August 2022, we measured longitudinal strain rate along the cable using a Silixa iDAS v2 interrogator with 10 m gauge length. Thanks to an average borehole inclination of ~3°, the cable was frictionally coupled to the borehole wall, providing high-quality recordings of seismic body waves that originated from active-shot experiments (16). In addition to these, the DAS cable recorded a large variety of natural englacial seismicity, including small individual events as well as event cascades that lasted for several seconds.

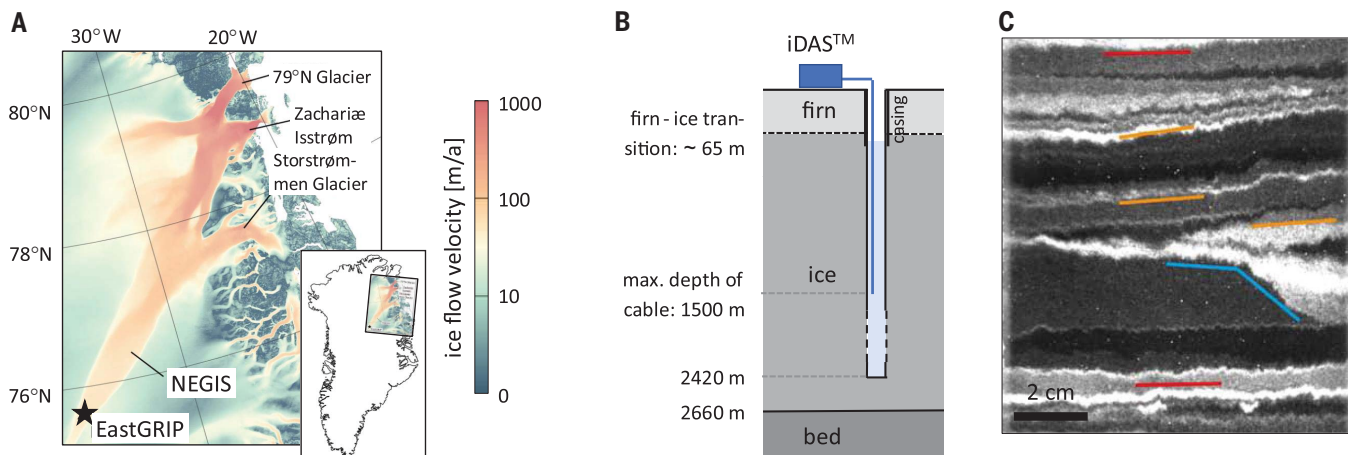
## Phenomenology

The borehole DAS recordings from 10 August 2022 contain five clear seismic event sequences, possibly representing the dynamic process

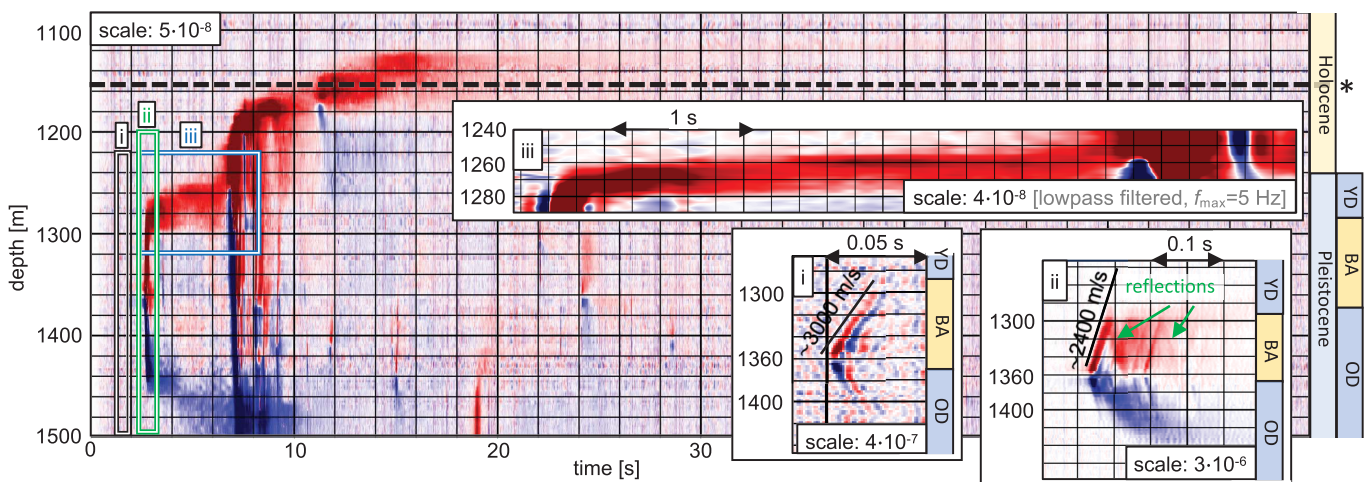
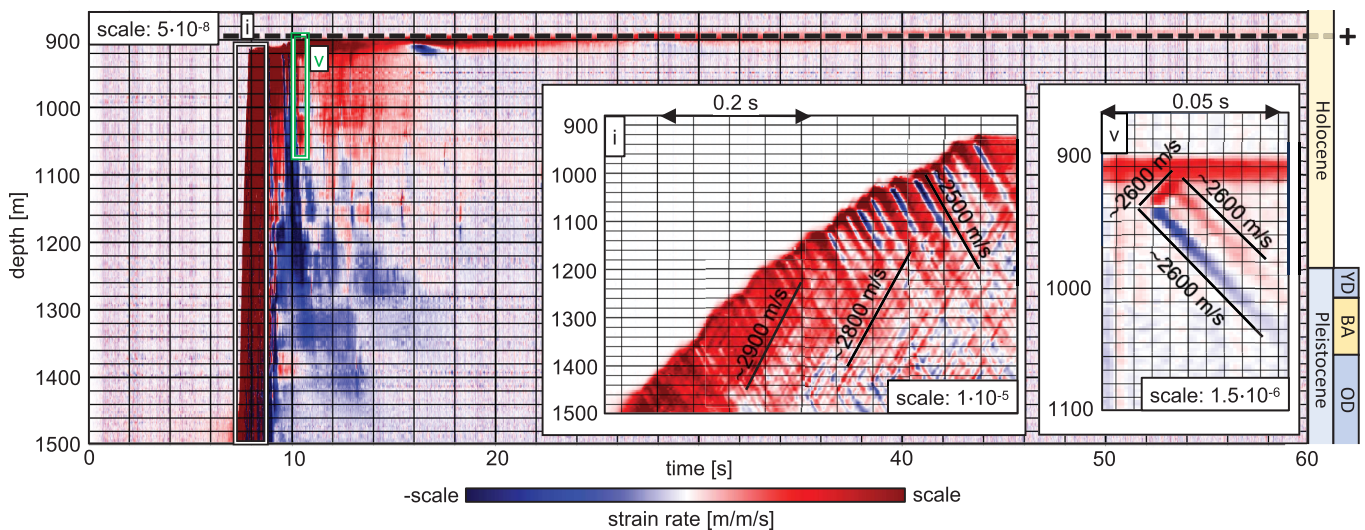
Downloaded from https://www.science.org at University Van Amsterdam on April 13, 2025

<sup>1</sup>Department of Earth and Planetary Sciences, ETH Zurich, Zurich, Switzerland. <sup>2</sup>Alfred-Wegener-Institut Helmholtz-Zentrum für Polar- und Meeresforschung, Bremerhaven, Germany. <sup>3</sup>Research School of Earth Sciences, The Australian National University, Acton, Canberra, Australia. <sup>4</sup>Niels Bohr Institute, University of Copenhagen, Copenhagen, Denmark. <sup>5</sup>Swiss Federal Research Institute WSL, Birmensdorf, Switzerland. <sup>6</sup>Laboratory of Hydraulics, Hydrology and Glaciology VAW, ETH Zurich, Zurich, Switzerland. <sup>7</sup>Université Côte d'Azur, IRD, CNRS, Observatoire de la Côte d'Azur, Geoazur Laboratory, Sophia Antipolis, Valbonne, France. <sup>8</sup>Université de Strasbourg/CNRS, Institut Terre et Environnement de Strasbourg, UMR7063, Strasbourg Cedex, France. <sup>9</sup>Fachbereich Geowissenschaften, Universität Bremen, Bremen, Germany.

\*Corresponding author. Email: andreas.fichtner@eaps.ethz.ch



**Fig. 1. Experimental setting.** (A) The Northeast Greenland Ice Stream (NEGIS) and its outlet glaciers shown in the form of surface flow velocities (41). (B) Schematic, not-to-scale illustration of the experimental setup. The DAS cable (blue line) reached a maximum depth of 1500 m inside the 2420-m-deep borehole within the 2660-m-deep ice (58). A Silixa iDAS v2 interrogator was used to perform measurements at a 1 kHz sampling rate and with 1-m channel spacing. (C) Optical line scan image of a structure similar to geological thrust faults yet only partly visible because of the narrow diameter of the ice core. The sample is from 1690.65 m depth. Colored lines indicate the ramp (blue), general layering of the section (red), and changed layer tilt inside the structure (orange). [Figure was modified from (15).]

**A** event sequence 1 [UTC 2022.08.10 12:19:36]**B** event sequence 2 [UTC 2022.08.10 12:27:22]

**Fig. 2. DAS recordings of seismic events. (A and B)** Sequences (A) 1 and (B) 2 are shown. The asterisk indicates the depth of the Saksunarvatn tephra (Grimsvötn) dated at 10.2 ka b2k, and the plus sign indicates the depth of the Mt. Mazama tephra (Crater Lake) dated at 7.6 ka b2k. (supplementary materials, section S3.1) Here and in Figs. 3 to 5, positive strain rates correspond to extension along the cable, and negative strain rates correspond to shortening.

Values for the color scale ranges are provided in the insets. For notational consistency, selected close-ups are labeled in the same way in figs. S1 and S2. (For example, close-ups and subevents ii to iv for sequence 2 that are not shown here are shown in fig. S2.) Abbreviations in the geologic time scales to the right are YD, Younger Dryas/GS-1 stadial; BA, Bølling-Allerød/GI-1 interstadial; and OD, Oldest Dryas/GS-2 stadial (59).

behind the brittle deformation patterns observed in the EastGRIP ice core. A visual summary of the sequences is shown in Figs. 2 and 3. This is complemented by a more comprehensive data survey in figs. S1 to S4. To tie borehole depth to age, we used the EastGRIP ice chronology of (7). Such conversions are indicated in thousand years before 2000 (ka b2k), which uses the year 2000 CE as origin.

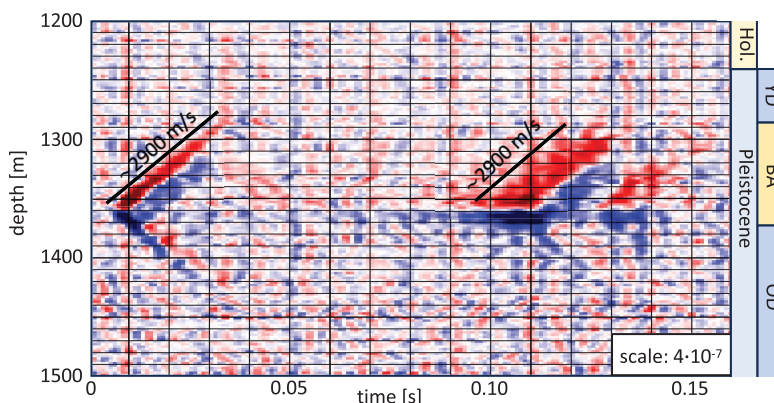
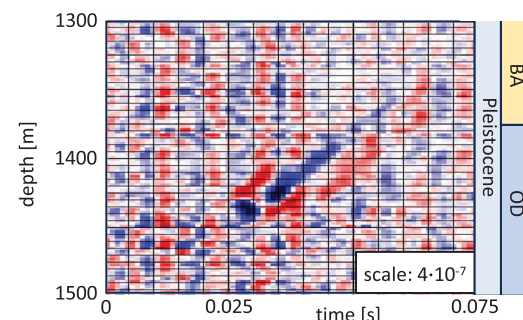
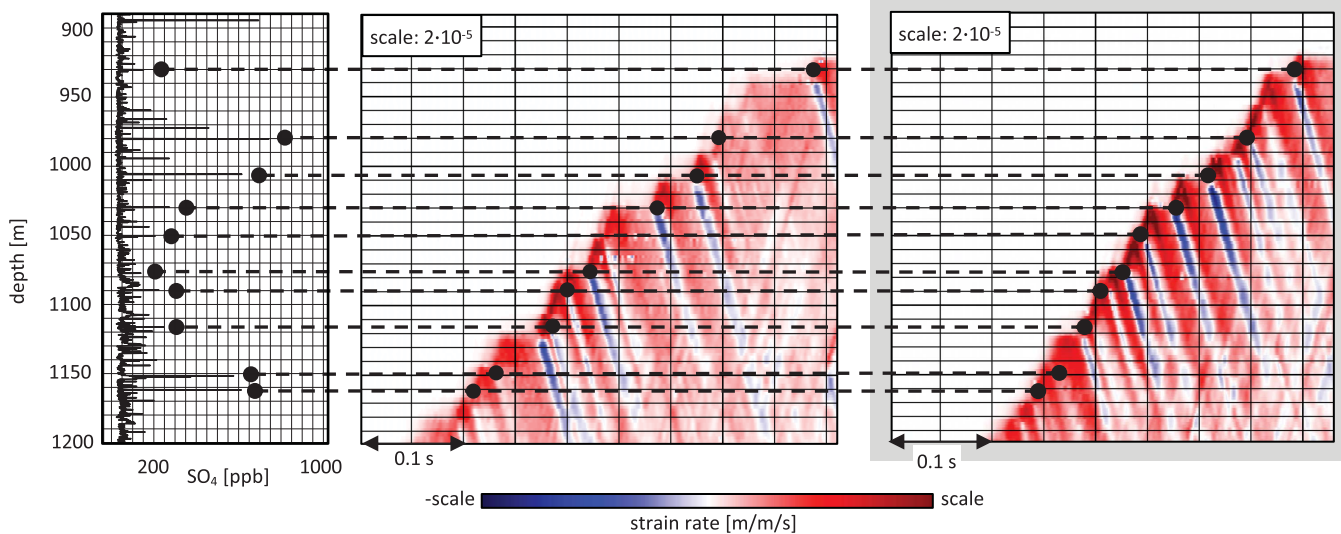
The sequences, with one to more than 100 subevents, have several characteristic properties. Most clearly, all subevents have a radiation pattern that is antisymmetric in the vertical direction, regardless of their amplitude and location. The subevents generally start with

positive strain rates (extension in fiber direction) radiating up and negative strain rates (shortening in fiber direction) radiating down. The character of many of the subevents resembles plane waves, with apparent wave speeds ranging from 2000 to 3000 m/s, which is faster than the *S* wave speed (~1800 m/s) but slower than the *P* wave speed (~3800 m/s) in the ice around EastGRIP (76). Thus, they are oblique *S* waves. Within layers of 10 to 20 m thickness, we observed shortening that lasts up to tens of seconds (for example, Fig. 2A, iii) and may be interpreted as creep. These deforming layers seem to temporarily impede the upward propagation of the wave field and in some cases

lead to strong downward reflections, with a reflection coefficient of around 0.5 (for example, Fig. 2, A, ii, and B, v).

Despite their complexity, the initial high-amplitude parts of sequences 2 and 5 are notably similar (Fig. 3C). They are composed of an upward-migrating cascade of subevents that originate at identical depths in both sequences. Although each subevent of a cascade radiates a wave field downward, the upward radiation stops after a few tens of meters at a layer where creep occurs for 10 to 50 ms, before the next subevent initiates.

None of the sequences observed in the EastGRIP borehole was detected by the geophone

**A** event sequence 3 [UTC 2022.08.10 17:15:42]**B** event 4 [UTC 2022.08.10 17:22:12]**C** zoom into event sequence 5 [UTC 2022.08.10 17:36:42]

**Fig. 3. DAS recordings of seismic events.** (A) Sequence 3. (B) The isolated event 4. (C) Part of event sequence 5, which is nearly identical to sequence 2. For comparison of sequences 2 and 5, close-up views of both are shown next to each other. The initiation depths of subevents closely correspond to (left)

$\text{SO}_4$  peaks.  $\text{SO}_4$  was not measured on the EastGRIP core but was projected onto the EastGRIP depth scale from the GRIP2 dataset (supplementary materials, section S3.2). Abbreviations in the geologic time scales are the same as in Fig. 2.

array at the surface, with the closest geophone installed at a distance of 160 m from the borehole (supplementary materials, section S2). This lack of surface observability is consistent with the DAS data, which do not show wave propagation extending beyond the thin creeping layers, and explains the absence of similar observations in the literature. Although weak seismic reflectors have been mapped below EastGRIP (16), comparable strong reflections off the creeping layers, such as in subevents 1.i and 2.v, are not present in active-shot data recorded with DAS in the borehole (supplementary materials, section 3.1) (16). This result excludes known changes in fabric orientation (12) as the cause for these reflections. The depths of the creeping layers (Fig. 2, asterisk and plus sign) coincide with the depth of two tephra (glass component of volcanic ash) layers that were iden-

tified in the EastGRIP ice core: the Mt. Mazama (Crater Lake, USA) tephra dated at 7.6 ka b2k and the Saksunarvatn (Grimsvötn, Iceland) tephra dated at 10.2 ka b2k. (supplementary materials, section S3.2) In a similar context, we observed that many of the subevents in sequences 2 and 5 (Fig. 3C) initiated near depths where sulfate ( $\text{SO}_4$ ) spikes, caused by volcanic eruptions, have been inferred from a projection of GRIP2  $\text{SO}_4$  measurements onto the EastGRIP depth scale (supplementary materials, section S3.3). Numerous subevents—especially in sequences 1, 3, and 4—initiated at 1360 m depth, which is close to the abrupt transition around 14.7 ka b2k from the cold climate of the Oldest Dryas/GS-2 stadial to the milder Bølling-Allerød/GI-1 climatic period. Located at 1375 m depth, this transition is particularly sharp at EastGRIP and manifests itself by increasing ice crystal sizes (18) in response

to decreasing impurity content (for example, dust particles) by a factor of 10 to 100 (19). The end of the Bølling-Allerød/GI-1 at 12.9 ka b2k or 1284 m depth is close to the creeping layer in Fig. 2A, iii, and the occurrence of downward reflections in Fig. 2A, ii. It was preceded by a ~110-year cluster of elevated global volcanic activity that manifested itself in a dense series of  $\text{SO}_4$  spikes in Greenland ice cores (20, 21). Abrupt changes in crystallographic fabric orientation are not detectable at any of these depths, neither in ice-core observations nor radar-based inferences (12). We therefore excluded changes in fabric as a dominating contributor to the observed nucleation locations.

#### Source mechanisms and wave field simulations

We can also exclude that the events were cable waves, which are nearly monochromatic

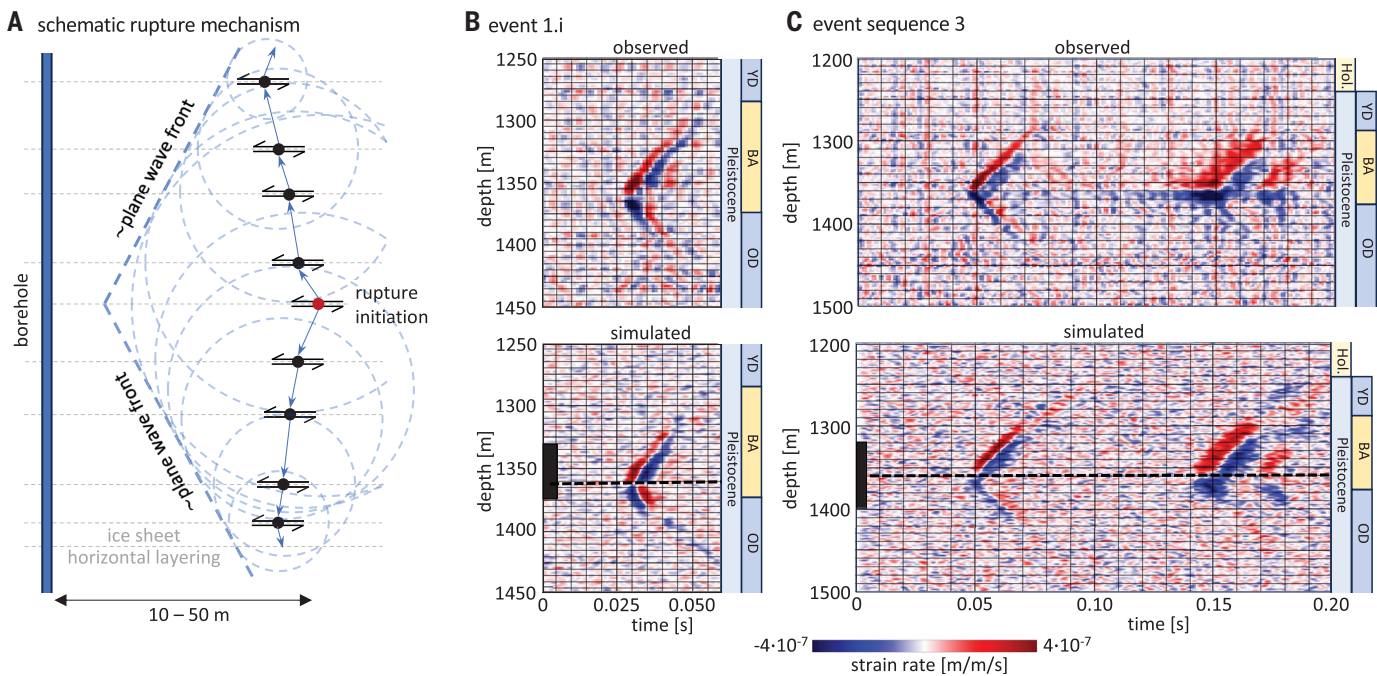


**Fig. 4. Comparison of observed and simulated DAS data.** (A) Cartoon illustration of a vertically oriented array of slip planes. Although their orientation cannot be inferred from the DAS data, they are drawn horizontally for simplicity. The red circle indicates the initiation point, from which subsequent ruptures were triggered in upward and downward directions. The superposition of circular wave fronts from the individual ruptures approximately produces a plane wave. (B and C) (Top) Observed and (Bottom) simulated DAS recordings of event 1.i and event sequence 3.

For a more realistic comparison, we added bandpass-filtered Gaussian noise to the simulations. The black bar in the simulation panels indicates the depth extent of the vertically oriented horizontal slip array, and the black dashed lines indicate the initiation depth. The exact moment density distributions used in the simulations are shown in figs. S14 and S16. For both event 1.i and sequence 3, the source array falls into the Bølling-Allerød/GI-1 depth range, which is characterized by climatically warmer and more viscous ice. Geologic time scale abbreviations are as in Fig. 2.

oscillations or traveling waves reflecting off the cable end (22, 23), which we did not observe. Furthermore, sequences 2 and 5 seem to have initiated below 1500 m depth, and sequence 1 seems to have propagated beyond 1500 m depth without evidence for upward reflections off the cable end. Correlations of initiation depths with  $\text{SO}_4$  content and tephra layers, as well as variable apparent wave speeds, make it even less likely that our observations are cable waves.

Using the approach detailed in the supplementary materials, section S4, we derived general source characteristics of the event sequences that explain key features listed above. The observed antisymmetric radiation pattern in the vertical direction constrains the range of possible fault orientations. In a cylindrical coordinate system—where  $r$  denotes distance to borehole axis,  $z$  is the depth, and  $\varphi$  is the azimuth—the diagonal moment tensor components  $M_{rr}$ ,  $M_{\varphi\varphi}$ , and  $M_{zz}$  produce symmetric radiation patterns and therefore can be excluded (supplementary materials, section S4.1). Wave fields excited by moment tensor components  $M_{r\varphi}$  and  $M_{z\varphi}$  cannot be observed with our experimental geometry. This implies that the sources must have a nonzero  $M_{rz}$  component, corresponding to either radially directed slip

on a horizontal fault or vertically directed slip on a vertical fault. Furthermore, the source location must be at some distance from the cable because an  $M_{rz}$  component source directly at the cable would not be observable. The data require the absence of an isotropic (explosive or implosive) component but are unable to constrain the precise orientation of the slip plane. Because brittle slip is likely to occur along pre-existing horizontal layers within the ice sheet, we continued to model the seismic sources as slip on a horizontal plane.

The vertically cascading sequences 2 and 5 hint at a generation mechanism of plane waves with variable apparent wave speeds, as recorded with the DAS system. As explained quantitatively in the supplementary materials, section S4.2.1, and illustrated schematically in Fig. 4A, a linear array of approximately vertically aligned horizontal fault planes that are triggered successively produces plane waves with an apparent wave speed controlled by the triggering speed and the inclination angle. Apparent wave speeds above the  $S$  wave speed can result from tilting the array toward the DAS cable and/or from  $P$  wave triggering, which has been previously observed for earthquakes (24). Successive excitation of ruptures on horizontal fault planes already allows us to explain less com-

plex parts of the recordings, such as subevent 1.i and sequence 3 (Fig. 4, B and C). In these and all subsequent simulations, sources at distances between 10 and 50 m from the borehole produce synthetic strain rate data that are compatible with the observations.

Large subevents in sequences 1, 2, and 5 caused creep that lasted up to several tens of seconds within thin layers, which produced strong reflections that are not present in the active surface shot data (16). The presence of such reflections may be explained by temporary fracturing or unwelding of an internal interface (Fig. 5A). In contrast to welded interfaces (25), nonwelded interfaces generate reflections and impede transmission in the absence of a material impedance contrast (26, 27). In the idealized case of a planar interface (supplementary materials, section S4.3), reflection and transmission coefficients can be derived analytically. The results indicate that a specific compliance of the interfaces on the order of  $10^{-9}$  to  $10^{-8}$  m/Pa can explain observed reflections off the strain accumulation layers and the resulting absence of surface observations of the event sequences. Less idealized distributions of nonwelded interfaces effectively behave as anisotropic layers, with reflection and transmission controlled by geometric properties of

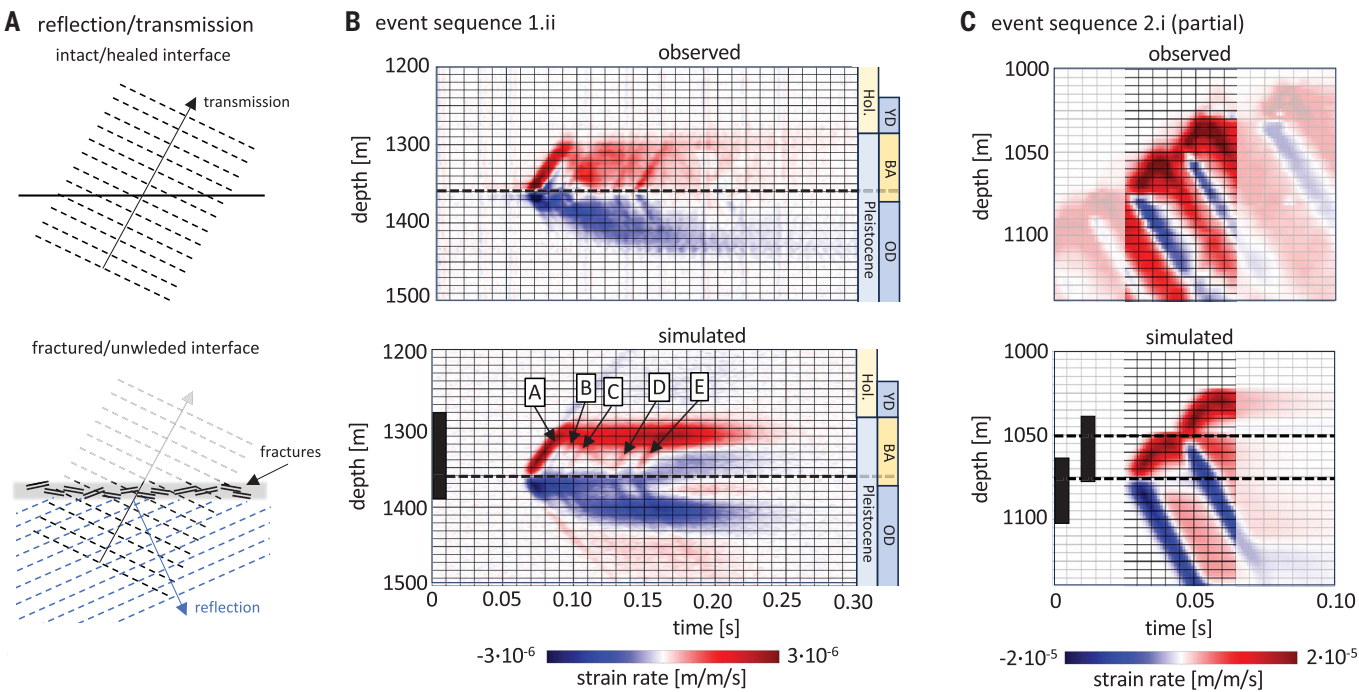


**Fig. 5. Comparison of observed and simulated sequences.** Shown are sequences 1.ii and 2.ii. (A) Cartoon illustration of wave transmission and reflection at (top) intact or healed and (bottom) fractured or unwelded interfaces. (B) and (C) Similar to Fig. 4, the black bars indicate the depth extent of the vertically oriented horizontal slip array, and the black dashed lines indicate the rupture initiation

depths. The exact moment density distributions used in the simulations are shown in figs. S16 and S17. The five subevents used to model sequence 1.ii are labeled "A" to "E." As for events 1.i and 3, the source array of sequence 1.ii falls into the Bølling-Allerød/GI-1 depth range. Geologic time scale abbreviations are as in Fig. 2.

the fractures, including their orientation and density (28, 29). A reflector at 1290 m depth allowed us to simulate the more complex event sequence 1.ii, consisting of at least five distinguishable subevents, some of which produce clearly visible reflections (Fig. 5B). Similarly, two subevents from sequence 2.ii are shown in Fig. 5C, simulated with reflectors at 1050 and 1025 m depth. Millimeter- to centimeter-scale fractures in ice have healing times on the order of tens to hundreds of seconds (30), which is consistent with our observation that active-shots data obtained several minutes after the natural events do not feature similar strong reflections.

Moment magnitudes ( $M_w$ ) estimated from DAS recordings of vertical strain  $\epsilon_{zz}$  range from  $M_w = -2.3$  for the foreshock 1.i to  $M_w = -0.24$  for the following main shock sequence 1.ii. They constrain the shear strain  $\epsilon_{xz}$  accumulated by a seismic cascade. Only ~10% of actual strain were transferred into the fiber (supplementary materials, section S5), meaning that estimated magnitudes are too low by ~0.67. Magnitude uncertainties are around  $\pm 0.5$ , primarily originating from uncertainties in the distance of the events from the cable and the inability to constrain  $M_{rp}$  and  $M_{zp}$ . The characteristic rupture size  $L$  can be deduced from  $M_w$ . Assuming that the stress drop  $\Delta\sigma$  is 10% of typical ice stream-driving stresses of

100 kPa (31), the circular-fault model  $L = (7M_0/16\Delta\sigma)^{1/3}$  (32) yields rupture sizes on the order of 1 to 10 m for our  $M_0$  estimates between  $\sim 3 \times 10^5$  and  $\sim 2 \times 10^8$  Nm. The application of Hooke's law,  $\Delta\sigma = \mu D/L$ , with shear modulus  $\mu \approx 2.8 \times 10^9$  Pa gives rupture displacements  $D$  on the order of tens to hundreds of micrometers. Applied to an individual event of sequence 2.ii (Fig. 5C), and taking the uncertainty in the moment estimate into account, this analysis yields  $D$  between  $5 \times 10^{-5}$  and  $2 \times 10^{-4}$  m per subevent. With  $N \approx 50$  subevents spread over a depth range of  $Z \approx 600$  m, a cascade such as 2.ii accumulates an average shear strain  $\epsilon_{xz} = ND/Z$  on the order of  $3 \times 10^{-6}$  to  $2 \times 10^{-5}$  m/m. A critical component of these estimates is the stress drop, which has a typical uncertainty of a factor of 10 for well-observed earthquakes (33). Adopting this uncertainty estimate for our case expands the range of  $\epsilon_{xz}$  to  $1 \times 10^{-6}$  to  $8 \times 10^{-5}$  m/m.

#### Implications for ice stream dynamics Relevance for ice stream deformation

Cascading englacial ice quakes cannot result from the presence of the borehole (supplementary materials, section S6). However, the characteristics of the events are not typical for glacial microseismicity, which is mostly associated with shear and tensile faulting near the surface and at the bed (34). Reported englacial

icequakes beneath the surface crevasse zone have tensile source mechanisms (35), in contrast to the events observed in this work. Tremor-like shear rupturing was located at the ice bed (36). Hence, cascading brittle failure within the ice may be particular to ice streams, where a vertical girdle crystallographic fabric forms to accommodate longitudinal extension (37, 38). The resulting anisotropy causes substantial hardening in the along-flow direction (13), which may result in brittle failure when stresses are sufficiently high.

The most conservative estimate of strain induced by the large cascade 2.ii,  $\epsilon_{xz} = 10^{-6}$  m/m, implies that around 100 of these event cascades may locally produce deformation that is comparable in amplitude with the  $10^{-4}$  m/m horizontal strain per year inferred from GPS measurements around EastGRIP (39). Although the relevance of englacial seismicity for large-scale ice stream deformation depends on its spatiotemporal distribution, our observing two large cascades within only 14 hours suggests that the phenomenon occurs rather frequently.

A similar long-term extrapolation can be made for the creeping deformation within thin layers. The largest-amplitude sequence 1.ii, for example, had average strain rates of  $\sim 5 \times 10^{-7}$  m/m/s that lasted for  $\sim 0.1$  s. Taking into account that only ~10% of the actual strain was transmitted into the fiber (supplementary

materials, section S5), we found that around 100 such events yielded vertical strain rates that are also on the order of  $10^{-4}$  year $^{-1}$ . However, without knowing the exact deformation style, an estimation of the corresponding horizontal strain is not possible.

At this stage, we may only speculate about the spatial distribution of seismic cascades. Radar sounding (40) and surface velocity observations (41) show that the internal ice structure and kinematics hardly vary over tens of kilometers around EastGRIP. The observed englacial seismicity is therefore unlikely to be a local peculiarity caused by local flow anomalies but instead is likely typical for the regional ice flow pattern. It seems plausible that seismic cascades are a common phenomenon in ice streams, but follow-up investigations are necessary for it to be confidently included in or excluded from ice sheet simulations.

### Bridging scales: From laboratory experiments to ice stream dynamics

Englacial seismic cascades near EastGRIP suggest that various properties and phenomena observed in laboratory experiments extrapolate to larger scales. Laboratory tests on mono- and polycrystalline ice show a distinct  $\text{SO}_4$ -induced reduction in viscosity resulting from increased dislocation density (42) and enhanced micro-cracking along grain boundaries (43). Near EastGRIP, these weaknesses promote creep over tens of microseconds, the nucleation of seismic events, and their vertical cascading over more than 600 m. Seismic cascades do not require the presence of pronounced tephra layers, which have not been observed near the large majority of  $\text{SO}_4$  peaks. However, when tephra with grain sizes in the tens of micrometers range, compared with the micrometer scale of background dust (44), is present it promotes creep over tens of seconds in thin layers and temporary unwelding that impedes the upward propagation of seismic waves. The underlying crystal-scale process may be impurity-induced grain-size reduction that causes the deformation mechanism to switch to grain-boundary sliding, which is known to enhance creep (45, 46). However, direct observations of cracks and deformation-related structures are challenging. Centimeter-scale fractures heal over time scales of minutes (30), and ice core samples are too small and too remote from the inferred location of the seismic cascades to provide constraints.

Experiments on single ice crystals have revealed dislocation avalanches that manifest themselves as long-term plasticity (47). These avalanches can trigger deformation cascades across grains that are hypothesized to be limited only by the laboratory system size (48). Our observations suggest that these microscopic cascades extend to ruptures at the tens of centimeter to meter scale, which then trig-

ger macroscopic seismic cascades across hundreds of meters. When averaged over large enough distances, this deformation style may still produce a smooth stress-strain curve, defining a representative volume element (RVE) for effective viscous deformation. Hence, our observation of seismic cascades propagating over at least 600 m implies that the RVE of ice stream ice is not at the centimeter scale but the kilometer scale.

### A plausible missing link: Implications for ice sheet modeling and future research

Our results imply that Glen's flow law for polycrystalline ice (49) is not applicable to ice stream modeling at spatial scales close to or smaller than the kilometer-size RVE. This flow law describes secondary creep over time scales longer than the Maxwell time, which itself is orders of magnitude longer than the seismogenic failure of the large-amplitude sequence Lii (34). Moreover, Glen's flow law is rate strengthening, whereas a rate-weakening rheology is necessary to produce dynamic instability during seismogenic deformation (50).

The magnitude of observed englacial seismicity suggests it as a plausible missing link between observed surface velocities in the upstream part of NEGIS and the results of current ice sheet models, which still fail to adequately reproduce the geometry and extent of NEGIS with the commonly used flow-law exponent of  $n = 3$  (51, 52).

At scales exceeding the RVE, the observed seismic deformation may be a process that contributes to the macroscopic effect of a larger exponent of around  $n = 4$ , which was recently proposed for fast-flowing regions of the Greenland and Antarctic ice sheets (53–55). However, to accurately model narrow ice streams, numerical resolutions as low as a few hundred meters are needed (56, 57), moving the grid spacing below the size of the RVE. Consequently, the impact of cascading seismicity on ice stream deformation should be considered to ensure reliable predictions of ice mass loss and sea level rise. This will require additional and longer borehole DAS experiments to better constrain the spatiotemporal distribution of the phenomenon; investigations on underlying crystal-scale processes; and modeling studies that constrain the interplay between englacial seismicity, rheology, and large-scale flow patterns.

### REFERENCES AND NOTES

- S. A. Khan et al., *Nat. Clim. Chang.* **4**, 292–299 (2014).
- M. D. King et al., *Commun. Earth Environ.* **1**, 1 (2020).
- H. Seroussi et al., *Cryosphere* **17**, 5197–5217 (2023).
- J. A. Church et al., *Climate Change 2013: The Physical Science Basis. Contribution of Working Group I to the Fifth Assessment Report of the Intergovernmental Panel on Climate Change* (Cambridge Univ. Press, 2013).
- C. Ritz et al., *Nature* **528**, 115–118 (2015).
- I. Joughin, B. E. Smith, C. G. Schoof, *Geophys. Res. Lett.* **46**, 4764–4771 (2019).
- E. Hartog, *An Introduction to Distributed Optical Fibre Sensors* (CRC Press, 2017).
- N. J. Lindsey, E. Martin, *Annu. Rev. Earth Planet. Sci.* **49**, 309–336 (2021).
- R. Greve, H. Blatter, *Dynamics of Ice Sheets and Glaciers* (Springer, 2009).
- E. Rignot, J. Mouginot, *Geophys. Res. Lett.* **39**, 2012GL051634 (2012).
- N. Stoll et al., *Cryosphere* **15**, 5717–5737 (2021).
- O. Zeising et al., *Cryosphere* **17**, 1097–1105 (2023).
- T. A. Gerber et al., *Nat. Commun.* **14**, 2653 (2023).
- K. R. McClay, Ed., *Thrust Tectonics* (Chapman & Hall, 1992), pp. 419–433.
- J. Westhoff, Visual stratigraphy of the EastGRIP ice core. thesis, University of Copenhagen, Niels Bohr Institute (2021).
- A. Fichtner et al., *Geophys. J. Int.* **235**, 2430–2441 (2023).
- S. Mojtabavi et al., *Clim. Past* **16**, 2359–2380 (2020).
- N. Stoll et al., *Cryosphere* **17**, 2021–2043 (2023).
- S. Schüpbach et al., *Nat. Commun.* **9**, 1476 (2018).
- A. Svensson et al., *Clim. Past* **16**, 1565–1580 (2020).
- P. M. Abbott et al., *Quat. Sci. Rev.* **274**, 107260 (2021).
- J. D. Munn, T. I. Coleman, B. L. Parker, M. J. Mondanos, A. Chalar, *J. Appl. Geophys.* **138**, 72–79 (2017).
- D. Mata Flores, E. D. Mercerat, J. P. Ampuero, D. Rivet, A. Sladen, *Geophys. J. Int.* **234**, 1389–1400 (2023).
- M. Vallée et al., *Earth Planet. Sci. Lett.* **601**, 117886 (2023).
- K. Aki, P. Richards, *Quantitative Seismology* (University Science Books, 2002).
- M. Schoenberg, *J. Acoust. Soc. Am.* **68**, 1516–1521 (1980).
- E. S. Krebes, *J. Canadian Soc. Expl. Geophys.* **23**, 66 (1987).
- E. Liu, J. A. Hudson, T. Pointer, *J. Geophys. Res.* **105** (B2), 2981–3000 (2000).
- S. Jin, A. Stovas, *Geophys. J. Int.* **222**, 260–288 (2020).
- A. Murdza, E. M. Schulson, C. E. Renshaw, A. Polojarvi, *Geophys. Res. Lett.* **49**, e2022GL099771 (2022).
- O. V. Sergienko, T. T. Creyts, R. C. A. Hindmarsh, *Geophys. Res. Lett.* **41**, 3925–3932 (2014).
- H. Kanamori, D. L. Anderson, *Bull. Seismol. Soc. Am.* **65**, 1073 (1975).
- R. E. Abercrombie, *Philos. Trans. A Math. Phys. Eng. Sci.* **379**, 20200131 (2021).
- E. A. Podolskiy, F. Walter, *Rev. Geophys.* **54**, 708–758 (2016).
- F. Walter et al., *Bull. Seismol. Soc. Am.* **99** (2A), 852–870 (2009).
- J. Umlauf et al., *Geophys. Res. Lett.* **48**, e2020GL090528 (2021).
- D. H. Richards, S. S. Pegler, S. Piazolo, N. Stoll, I. Weikusat, *J. Geophys. Res. Solid Earth* **128**, e2023JB027245 (2023).
- D. A. Lilien, N. M. Rathmann, C. S. Hvidberg, D. Dahl-Jensen, *J. Geophys. Res. Earth Surf.* **126**, e2021JF006306 (2021).
- C. S. Hvidberg et al., *Cryosphere* **14**, 3487–3502 (2020).
- S. Franke et al., *Earth Syst. Sci. Data* **14**, 763–779 (2022).
- I. Joughin, B. E. Smith, I. M. Howat, *J. Glaciol.* **64**, 1–11 (2018).
- Y. L. Trickett, I. Baker, P. M. S. Pradhan, *J. Glaciol.* **46**, 239–243 (2000).
- K. Hammonds, I. Baker, *J. Geophys. Res. Earth Surf.* **123**, 535–556 (2018).
- J. P. Steffensen, *J. Geophys. Res.* **102** (C12), 26755–26763 (1997).
- D. L. Goldsbys, D. L. Kohlstedt, *J. Geophys. Res.* **106** (B6), 11017–11030 (2001).
- M. D. Behn, D. L. Goldsbys, G. Hirth, *Cryosphere* **15**, 4589–4605 (2021).
- J. Weiss, J. R. Grasso, *J. Phys. Chem. B* **101**, 6113–6117 (1997).
- J. Weiss, *Philos. Trans. A Math. Phys. Eng. Sci.* **377**, 20180260 (2019).
- E. M. Schulson, P. Duval, *Creep and Fracture of Ice* (Cambridge Univ. Press, 2009).
- C. H. Scholz, *Nature* **391**, 37–42 (1998).
- A. Aschwanden, M. A. Fahnestock, M. Truffer, *Nat. Commun.* **7**, 10524 (2016).
- M. Rückamp, R. Greve, A. Humbert, *Polar Sci.* **21**, 14–25 (2019).
- F. Gillet-Chaulet, R. C. A. Hindmarsh, H. F. J. Corr, E. C. King, A. Jenkins, *Geophys. Res. Lett.* **38**, n/a (2011).
- P. D. Bons et al., *Geophys. Res. Lett.* **45**, 6542–6548 (2018).
- J. D. Millstein, B. M. Minchew, S. S. Pegler, *Commun. Earth Environ.* **3**, 57 (2022).
- E. Bueler, *J. Glaciol.* **62**, 230–242 (2016).
- A. Aschwanden et al., *Sci. Adv.* **5**, eaav9396 (2019).
- P. Valverde et al., *Cryosphere* **8**, 1275–1287 (2014).
- S. O. Rasmussen et al., *Quat. Sci. Rev.* **106**, 14–28 (2014).
- A. Fichtner, Hidden cascades of seismic ice stream deformation - raw data. Zenodo (2025); <https://doi.org/10.5281/zenodo.14811755>.

**ACKNOWLEDGMENTS**

We gratefully acknowledge the careful and constructive comments of four anonymous reviewers who helped us to sharpen our line of arguments. Our experiment would not have been possible without the immense technical support by S. Børsting, S. Hilmarson, and D. Dahl-Jensen. Invaluable technical support, before and during the experiment, was provided by Silixa (A. Chalari and support team) and Solifos (A. Fasciati). We gratefully acknowledge valuable discussions with R. Alley, D. Dahl-Jensen, T. Dahl-Jensen, S. Fishwick, T. Hudson, B. Lipovsky, R. Pevzner, H. Seroussi, and L. Zoet. O.E. and D.Z. thank M. Bes de Berc for preparing the seismic nodes and managing the associated data. **Funding:** O.E. and D.Z. were supported by the CHIPS grant of the University of Strasbourg Institute for Advanced Studies, the French Europe and Foreign Affair ministry, the French Higher Education and Research ministry, the German Ministry for Education and Research, and the German Academic Exchange Service (DAAD) under the project number 49360YJ-PHC PROCOPE 2023. EastGRIP is directed and

organized by the Centre for Ice and Climate at the Niels Bohr Institute, University of Copenhagen. It is supported by funding agencies and institutions in Denmark (A. P. Møller Foundation, University of Copenhagen), the United States (US National Science Foundation, Office of Polar Programs), Germany (Alfred Wegener Institute, Helmholtz Centre for Polar and Marine Research), Japan (National Institute of Polar Research and Arctic Challenge for Sustainability), Norway (University of Bergen and Trond Mohn Foundation), Switzerland (Swiss National Science Foundation), France (French Polar Institute Paul-Emile Victor, Institute for Geosciences and Environmental Research), Canada (University of Manitoba), and China (Chinese Academy of Sciences and Beijing Normal University). **Author contributions:** A.F.: data acquisition, formal data analysis, and interpretation. C.H.: data acquisition and interpretation. B.L.N.K.: formal data analysis. A.S., J.W., J.-P.A., E.C., D.Z., D.J., and O.E.: interpretation of results and linkage to non-seismic data. F.W.: formal data analysis and interpretation. All authors contributed to writing and revision. **Competing interests:** The authors declare no competing interests. **Data and materials**

**availability:** All data presented in this paper, as well as Python code to read and visualize them, is available on Zenodo (60).

**License information:** Copyright © 2025 the authors, some rights reserved; exclusive licensee American Association for the Advancement of Science. No claim to original US government works. <https://www.science.org/about/science-licenses-journal-article-reuse>

**SUPPLEMENTARY MATERIALS**

[science.org/doi/10.1126/science.adp8094](https://science.org/doi/10.1126/science.adp8094)

Materials and Methods

Supplementary Text

Figs. S1 to S21

References (61–82)

Submitted 17 April 2024; accepted 21 January 2025

Published online 6 February 2025

[10.1126/science.adp8094](https://doi.org/10.1126/science.adp8094)

Correction (3 March 2025): The Acknowledgments have been updated to recognize support from the German Ministry for Education and Research and the German Academic Exchange Service (DAAD).